Sensors & Diagnostics

PAPER

View Article Online
View Journal | View Issue

Cite this: *Sens. Diagn.*, 2025, **4**, 984

Surface-modified titanium carbide MXene as an effective platform for the immobilization of toluidine blue and H_2O_2 biomarker detection in biological samples

Devarasu Mohanapriya and Kathavarayan Thenmozhi *

The development of reliable and cost-effective electrochemical sensors for hydrogen peroxide (H_2O_2) monitoring is crucial in biomedical diagnostics, especially in early disease diagnosis. Herein, we prudently synthesized an acid-functionalized COOH–$Ti_3C_2T_x$ MXene, onto which a toluidine blue (TB) redox mediator was covalently immobilized and employed for the distinctive determination of H_2O_2. The synthesized COOH–$Ti_3C_2T_x$ MXene is coated over a glassy carbon electrode (GCE), followed by the covalent immobilization of the electroactive TB dye through the *N*-(3-dimethylaminopropyl)-*N*′-ethylcarbodiimide hydrochloride (EDC)/*N*-hydroxysuccinimide (NHS) coupling reaction. This in turn results in the firm anchoring of the TB dye by establishing a stable amide linkage between the –COOH group of COOH–$Ti_3C_2T_x$ and the free –NH_2 group of TB. Thus, the obtained TB/COOH–$Ti_3C_2T_x$/GCE sensor demonstrates an excellent electrocatalytic response for H_2O_2 determination over a broad linear range of 5 μM to 100 μM and 100 μM to 1.1 mM with a high sensitivity of 0.61 μA μM^{-1} cm^{-2} and a low detection limit of 1.5 μM. Notably, the fabricated electrode demonstrated exceptional stability and reproducibility as well as high selectivity and sensitivity in the detection of H_2O_2. Furthermore, the developed sensor showed very good recovery towards the detection of H_2O_2 in milk and serum samples. The attained analytical performance is attributed to the improved electrical wiring between the TB mediator and the conductive MXene platform.

Received 26th June 2025,
Accepted 19th August 2025

DOI: 10.1039/d5sd00114e

rsc.li/sensors

1. Introduction

Hydrogen peroxide (H_2O_2) is one of the most important by-products of metabolic processes in the human body and plays a major role in various physiological functions. However, the excessive production of H_2O_2 can have a detrimental effect on the brain and tissues, which might lead to several life-threatening issues, such as cardiovascular diseases, Alzheimer's disease and cancer.[1–4] Accordingly, H_2O_2 is regarded as a distinctive biomarker for the early diagnosis of various diseases, including Alzheimer's disease, asthma, chronic obstructive pulmonary disease, Parkinson's disease, cancer and periodontitis, and thus, the simple, cost-effective, sensitive and accurate detection of H_2O_2 becomes necessary. H_2O_2 has been detected thus far using various quantification techniques such as spectrophotometry, fluorescence, titrimetry, resonance light scattering and chemiluminescence. Unfortunately, many of these techniques are costly, time-consuming and complicated, limiting their application in monitoring H_2O_2 in real-time samples.[5–8] Among the several methods, the electrochemical determination of H_2O_2 is strongly recommended because of its ease of sample preparation, affordability, sensitivity and selectivity.[9,10] In recent years, the electrocatalytic detection of H_2O_2 has been extensively researched using numerous modified electrodes to address its oxidation or reduction. Amongst these, enzymatic electrochemical biosensors have the benefits of excellent sensitivity and selectivity.[11–13] In contrast, their application is restricted owing to the expensive nature of enzymes, laborious immobilization processes, poor repeatability and environmental instability.[14]

Non-enzymatic electrochemical sensors have been utilized as an efficient alternative for biosensors since they not only enhance the durability of the sensor, but also enable the detection of H_2O_2 at low potentials.[15] These non-enzymatic sensors can be prepared through electrochemical pre-treatment, polymerization, mediator adsorption or self-assembly and covalent immobilization of mediators over a conductive substrate.[11] Mediators often include organic salts,

Department of Chemistry, School of Advanced Sciences, Vellore Institute of Technology (VIT), Vellore-632014, India. E-mail: k.thenmozhi@vit.ac.in, kt.thenmozhi@gmail.com

metal complexes, quinones, catechols and redox dyes. However, electrodes fabricated by a simple adsorption process would quickly lose their electrocatalytic activity due to the lack of proper immobilization.[16,17] The technique utilized to immobilize the mediators is a crucial step in the fabrication of modified electrodes and has a significant impact on the sensitivity and stability of the sensor. Thus, the covalent immobilization of mediators is the most appropriate technique to prepare highly stable, leak-free sensors.[18] Organic dye molecules like azure A, methylene blue, methylene green and toluidine blue (TB) have been employed as mediators to investigate the electrocatalytic reduction of H_2O_2 owing to their well-defined redox behaviour, which facilitate the electron transfer during the electrochemical process.[19,20] TB has been chosen as a mediator for this study because of its well-defined redox behaviour at lower potentials, good electrochemical stability and potential to boost the electron transfer between the electrode and the electrolyte interface.[21] The major drawback of using TB or other similar dye-based electrochemical sensors over an extended period is that they gradually disintegrate from the electrode surface owing to their water solubility, resulting in the fouling of the electrode along with subsequent loss in sensitivity and durability. This limitation can be resolved *via* the covalent anchoring of these redox dyes/mediators on a stable substrate.[22] The development of sensors for ambient or *in vivo* analysis requires such careful consideration of this immobilization aspect.

The choice of an appropriate substrate material to immobilize the redox mediator is crucial for developing a successful sensor. Novel 2D single-layer transition metal carbide and nitride MXene nanosheets (NSs) have become popular as a potential host material for electrochemical sensors compared to existing 2D materials such as graphene oxide (GO), graphitic carbon nitride (g-C_3N_4) and multi-walled carbon nanotubes (MWCNTs).[23–27] Specifically, in the family of 2D MXenes, the titanium carbide MXene ($Ti_3C_2T_x$) has been well explored for various applications by virtue of its intriguing properties such as excellent conductivity, high surface area, outstanding electrochemical stability and good hydrophilicity.[28,29] Because terminal groups account for most of the characteristics of $Ti_3C_2T_x$, prudently designing these $Ti_3C_2T_x$ MXenes with functional groups such as –COOH and –NH_2 can advantageously aid in the covalent immobilization of dye molecules.[30]

To the best of our knowledge, no efforts have been made so far to fabricate a disintegration-free electrochemical sensor for the detection of the H_2O_2 biomarker using TB and acid-functionalized MXene (COOH–$Ti_3C_2T_x$). This prompted us to fabricate an electrochemical sensor for H_2O_2 detection through the covalent immobilization of TB over COOH–$Ti_3C_2T_x$ MXene. In this regard, the redox-active TB was coupled with the COOH–$Ti_3C_2T_x$ NSs *via* the *N*-(3-dimethylaminopropyl)-*N*′-ethylcarbodiimide hydrochloride (EDC)/*N*-hydroxysuccinimide (NHS) coupling reaction, which led to the stable anchoring of TB. Additionally, the constructed electrochemical sensor demonstrated a broad detection range and good sensitivity towards H_2O_2 detection. The synthesized surface-functionalized $Ti_3C_2T_x$ proved to be a great anchoring site for mediator immobilization, and thus, the constructed sensor was highly stable and reproducible. This is of great significance as the lack of effective immobilization would result in diminished current response because of the dissolution of the water-soluble TB in the aqueous electrolyte. Furthermore, the fabricated electrochemical sensor demonstrated remarkable electrochemical performance for the determination of H_2O_2 in milk and serum samples, providing an effective approach towards early disease diagnosis.

2. Experimental section

All chemicals and instrumentation details are given in the (SI).

2.1. Synthesis of $Ti_3C_2T_x$ NSs

In this study, we synthesized $Ti_3C_2T_x$ NSs using a safer and more environmentally friendly *in situ* HF wet acid etching method that we have reported previously.[31,32] Typically, as illustrated in Fig. 1a, 1 g of the Ti_3AlC_2 MAX phase powder was slowly added to an etching solution that consisted of 1 g of lithium fluoride (LiF) and hydrochloric acid (9 M HCl). The mixture was stirred for 24 h at room temperature (RT) to remove the Al layer from Ti_3AlC_2. Thereafter, the resulting mixture was washed with deionized water by centrifugation until the pH of the solution reached 6. Following that, the obtained solution was subjected to ultrasonication for 1 h in a N_2 atmosphere to get homogenously dispersed $Ti_3C_2T_x$ NSs. Later, the sample was freeze-dried at −60 °C and stored in a vacuum desiccator for further characterization.

2.2. Synthesis of COOH–$Ti_3C_2T_x$ NSs

After the successful preparation of $Ti_3C_2T_x$ NSs comprising terminal –OH functional groups, we further intended to functionalize these $Ti_3C_2T_x$ NSs with –COOH functional groups, which in turn will be beneficial for the covalent immobilization of redox dye molecules. The readily reactive –OH groups were subjected to ring-opening, followed by an esterification reaction with succinic anhydride, which enabled the introduction of carboxylic acid functional groups onto the $Ti_3C_2T_x$ NS surface to produce acid-functionalized MXene (COOH–$Ti_3C_2T_x$) NSs (Fig. 1a). Specifically, 0.5 g of $Ti_3C_2T_x$ NSs was dispersed in 25 mL of ethanol using ultrasonication. Meanwhile, 5 g of succinic anhydride was added to 25 mL of ethanol and transferred to the $Ti_3C_2T_x$ NS-ethanol mixture, and the reaction mixture was kept under constant stirring at 300 rpm for 48 h.[33] The obtained precipitate was rinsed

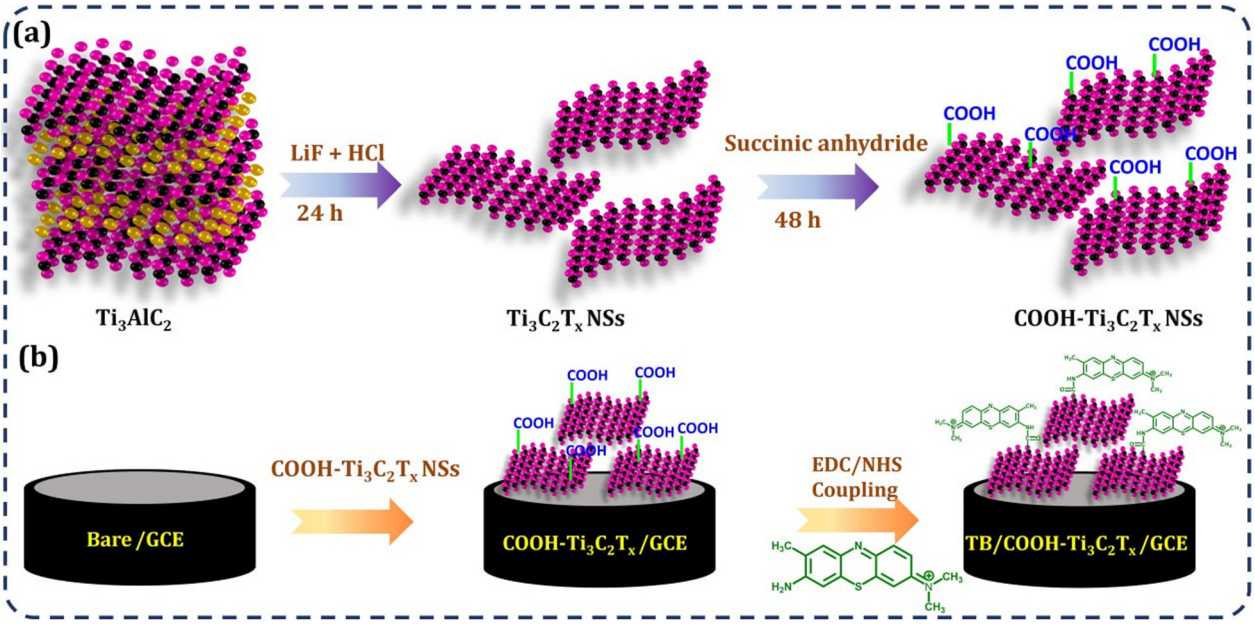

Fig. 1 (a) Schematic representation of the synthesis of $Ti_3C_2T_x$ NSs and COOH–$Ti_3C_2T_x$ NSs. (b) Stepwise fabrication of the TB/COOH–$Ti_3C_2T_x$/GCE.

thoroughly with DI water and centrifuged at 3000 rpm until all the remaining residual succinic anhydride was removed. Afterwards, the centrifugate was vacuum-dried for 12 h at 25 °C to obtain COOH–$Ti_3C_2T_x$ NSs.

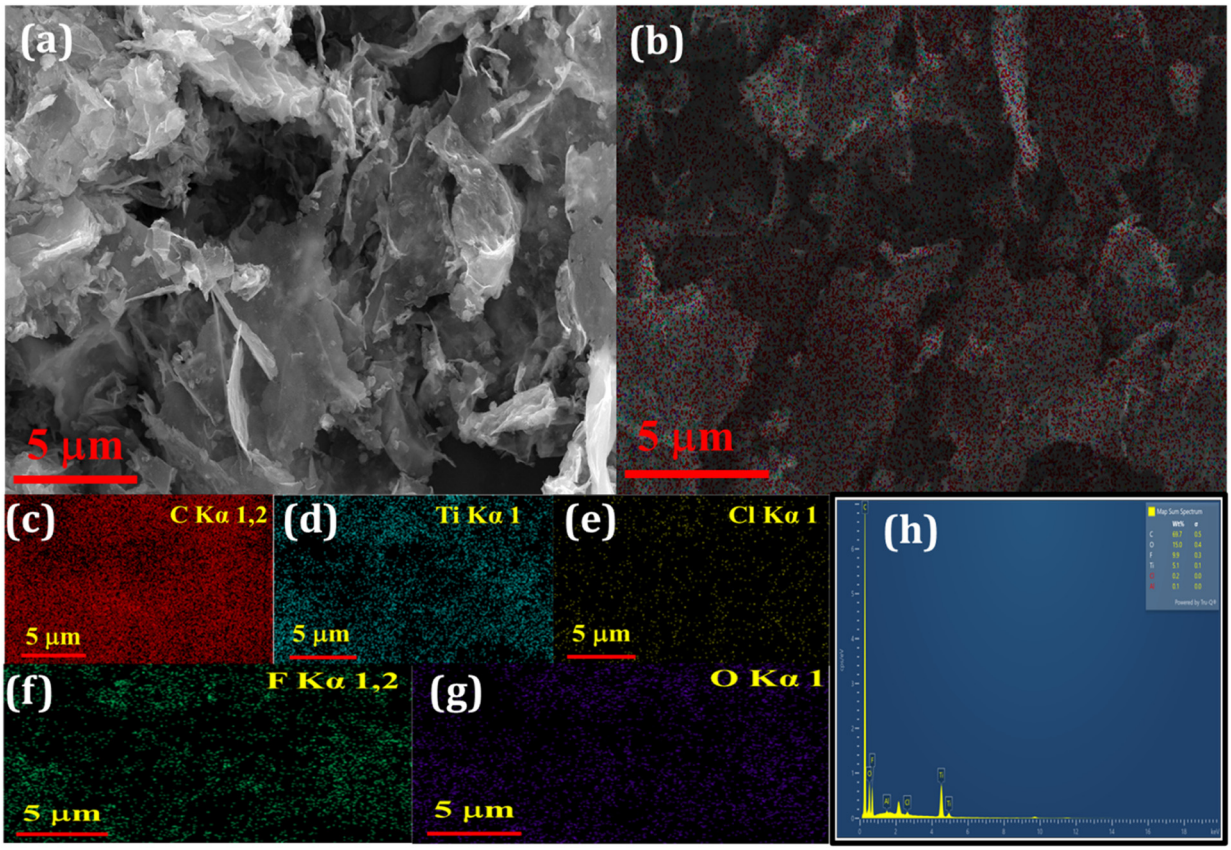

Fig. 2 (a) FESEM image, (b–g) elemental mappings and (h) EDX analysis of COOH–$Ti_3C_2T_x$ NSs.

2.3. Sensor fabrication through the covalent immobilization of TB on the COOH–$Ti_3C_2T_x$ platform

The TB-modified electrode was prepared according to the following steps. Initially, a bare glassy carbon electrode (GCE) was polished thoroughly using an alumina powder and ultrasonicated using ethanol and water mixture for 5 min to achieve a mirror-clean electrode surface. Thereafter, 10 μL of COOH–$Ti_3C_2T_x$ NSs (2 mg in 200 μL of ethanol) was drop-casted on top of the polished electrode. After drying, the carboxyl groups present on the $Ti_3C_2T_x$ NSs were further activated using 5 μL of 2 mM EDC in 0.1 M phosphate buffer solution (PBS), followed by 5 μL of 5 mM NHS in 0.1 M PBS for 60 min each. Thereafter, the modified electrode was dipped in a TB solution (2 mg in 0.5 mL ethanol) for 1 h to facilitate the covalent immobilization of the redox mediator. Further, the fabricated TB/COOH–$Ti_3C_2T_x$/GCE was washed gently with PBS to remove loosely adsorbed TB. Then, 5 μL of 1% Nafion was coated over the constructed TB/COOH–$Ti_3C_2T_x$/GCE to enhance the stability.

3. Results and discussion

3.1. Characterization of $Ti_3C_2T_x$ and COOH–$Ti_3C_2T_x$ NSs

The morphologies and elemental compositions of the Ti_3AlC_2, $Ti_3C_2T_x$ NSs and COOH–$Ti_3C_2T_x$ NSs were probed using field-emission scanning electron microscopy (FESEM) and scanning electron microscopy (SEM) with elemental mapping. The MAX phase precursor Ti_3AlC_2 demonstrates the closed layered structure comprising Al and is displayed in Fig. S1. By contrast, the synthesized $Ti_3C_2T_x$ NSs reveal a well-separated NS-like morphology, which indicates the effective etching of Al from Ti_3AlC_2 (Fig. S2a and b). Fig. S2c–h depicts the elemental mapping of $Ti_3C_2T_x$ NSs, which explicitly witnesses the removal of Al from the precursor and also shows the uniform distribution of all other elements. The FESEM images of COOH–$Ti_3C_2T_x$ NSs in Fig. 2a and b further exhibit the NS-like morphology, which proves that the surface morphology remains unaltered during surface functionalization. Further, the decrease in the wt% of other functional groups like –F and –Cl on COOH–$Ti_3C_2T_x$ NSs may be due to the successful replacement of the –COOH groups on $Ti_3C_2T_x$ NSs

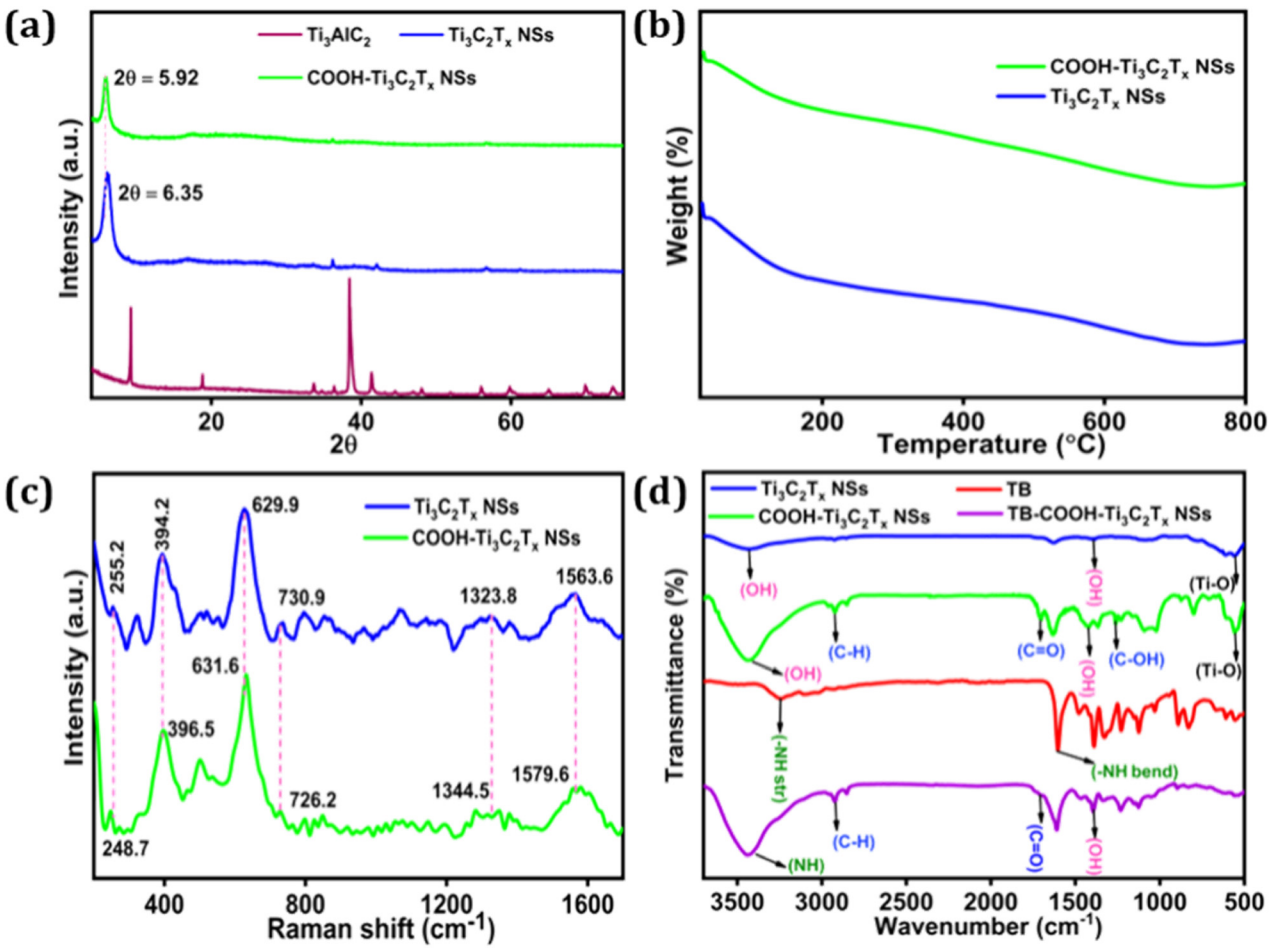

Fig. 3 (a) XRD patterns of Ti_3AlC_2, $Ti_3C_2T_x$ NSs and COOH–$Ti_3C_2T_x$ NSs. (b) TGA curves of $Ti_3C_2T_x$ NSs and COOH–$Ti_3C_2T_x$ NSs. (c) Raman spectra of $Ti_3C_2T_x$ NSs and COOH–$Ti_3C_2T_x$ NSs. (d) FTIR spectra of $Ti_3C_2T_x$ NSs, COOH–$Ti_3C_2T_x$ NSs, TB and TB/COOH–$Ti_3C_2T_x$ NSs.

(Fig. 2h). In addition, the elemental analysis of COOH–$Ti_3C_2T_x$ NSs also confirms the absence of Al and the uniform dispersion of the other elements (Fig. 2c–g).

The powder X-ray diffraction (XRD) technique was utilized to analyse the crystal structures of the $Ti_3C_2T_x$ and COOH–$Ti_3C_2T_x$ NSs, and the results are depicted in Fig. 3a. The XRD pattern of $Ti_3C_2T_x$ indicates the formation of a characteristic peak at 6.3°, corresponding to (002), and a diminishing peak at 38.4°, corresponding to Al, confirming that $Ti_3C_2T_x$ NSs have been successfully synthesized. In the case of COOH–$Ti_3C_2T_x$ NSs, the (002) peak shifts towards a lower 2θ of 5.9°, and this may be due to the –COOH functionalization on the surface of $Ti_3C_2T_x$ NSs.[34] Further, the $Ti_3C_2T_x$ NSs and COOH–$Ti_3C_2T_x$ NSs were investigated using thermogravimetric analysis (TGA), and the results are displayed in Fig. 3b. After subjecting the samples to 900 °C, the obtained residual weights for $Ti_3C_2T_x$ and COOH–$Ti_3C_2T_x$ NSs were 82.6% and 78.1%, respectively.[35,36] The higher weight loss observed for COOH–$Ti_3C_2T_x$ NSs than that for $Ti_3C_2T_x$ NSs may be due to the functionalized –COOH groups on the surface of $Ti_3C_2T_x$. Acid functionalization was further confirmed by recording the Raman spectra of the synthesized $Ti_3C_2T_x$ and COOH–$Ti_3C_2T_x$ NSs, as illustrated in Fig. 3c. The Raman spectra of $Ti_3C_2T_x$ NSs show four significant peaks at 255.2, 394.2, 629.9 and 730.9 cm^{-1}, which are associated with $Ti_3C_2T_x$ NSs. These peaks correspond to the in-plane vibrations of Ti–C, O atoms, C atoms and surface functional groups, respectively.[37] Further, the peaks attributed to D and G bands (carbon atom defect peaks) are observed around 1323.8 and 1563.6 cm^{-1}, respectively.[38] After the functionalization of $Ti_3C_2T_x$ NSs with –COOH groups, a slight shift in the Raman peaks, along with an increase in their intensity, is observed in the spectrum of COOH–$Ti_3C_2T_x$ NSs, and this infers that the $Ti_3C_2T_x$ NSs have been functionalized with –COOH groups to a greater extent.[39]

The formation of COOH-functionalized $Ti_3C_2T_x$ NSs from the OH-terminated $Ti_3C_2T_x$ NSs was investigated using FTIR spectroscopy. The FTIR spectrum (Fig. 3d) of $Ti_3C_2T_x$ NSs (blue curve) displays the stretching and bending vibrations at 3434 cm^{-1} and 1374 cm^{-1}, respectively, confirming the strong –OH terminal group on the surfaces of $Ti_3C_2T_x$ NSs. In the case of COOH–$Ti_3C_2T_x$ NSs, the peak at 1628 cm^{-1} is due to the presence of the carbonyl group and the peak at 1251 cm^{-1} is the characteristic absorption peak of C–OH, confirming the presence of carboxylic group.[33] The peak at 1708 cm^{-1} can be ascribed to the ester group generated by succinic anhydride, and the strong peak at 2931 cm^{-1}

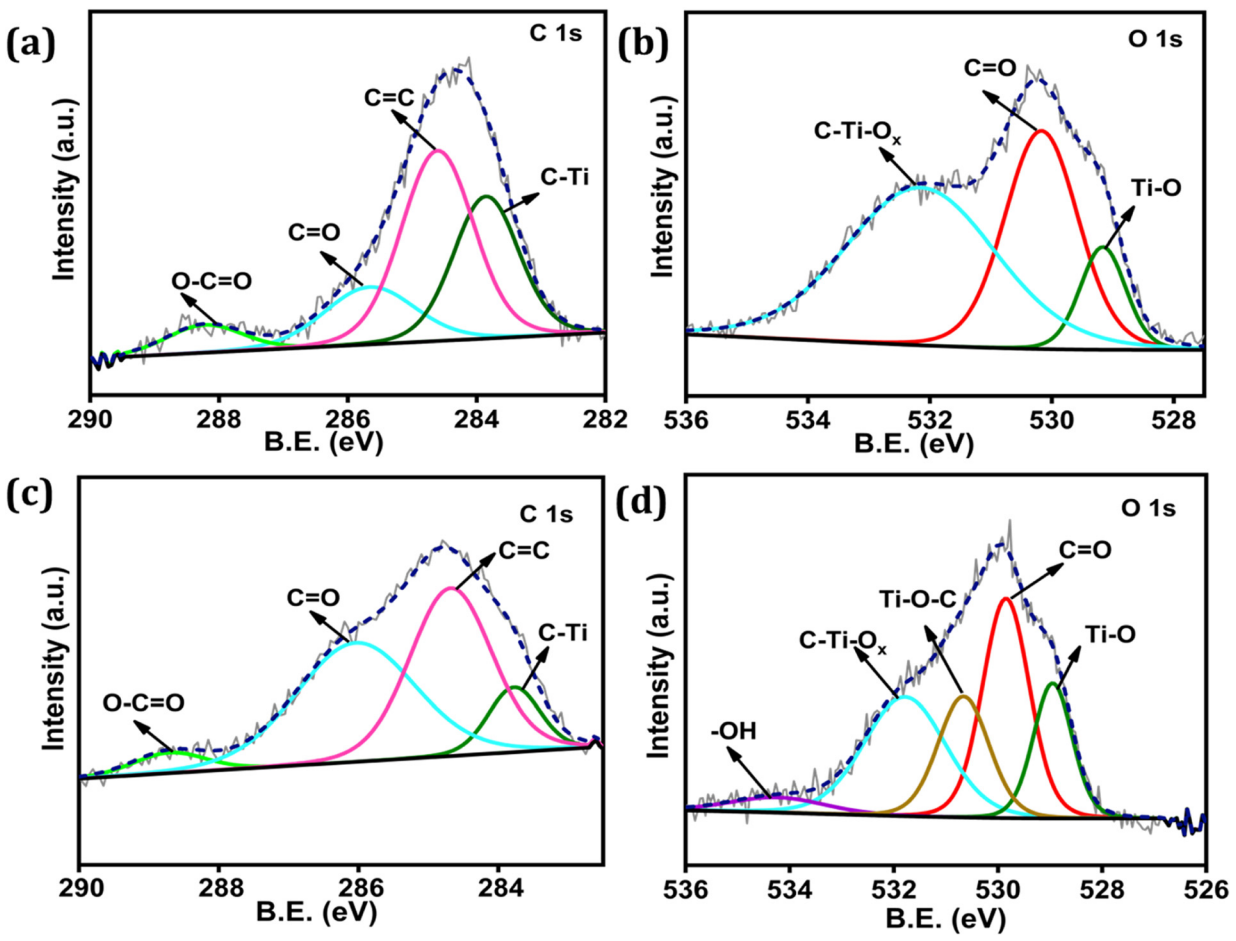

Fig. 4 C 1s and O 1s core-level XPS spectra of (a and b) $Ti_3C_2T_x$ and (c and d) COOH–$Ti_3C_2T_x$ NSs.

corresponds to the anti-symmetrical stretching vibration of C–H in COOH–$Ti_3C_2T_x$ NSs. Furthermore, after ring-opening and esterification reactions, the stretching vibration of Ti–O at 617 cm^{-1} shifts significantly to 563 cm^{-1}, which may be influenced by the conjugated groups connected *via* Ti–O bonds. The covalent anchoring of TB over COOH–$Ti_3C_2T_x$ NSs *via* amide bond formation between the free –NH_2 of TB and the –COOH of COOH–$Ti_3C_2T_x$ NSs is validated by the formation of new peaks at 3441 cm^{-1} and 1700 cm^{-1}, which represent the –NH and –C═O vibrations of amide groups formed, respectively.[40]

The nature and composition of surface elements on $Ti_3C_2T_x$ NSs and COOH–$Ti_3C_2T_x$ NSs were examined through X-ray photoelectron spectroscopy (XPS), and the detailed core-level spectra are illustrated in Fig. 4. The survey spectra of $Ti_3C_2T_x$ and COOH–$Ti_3C_2T_x$ NSs in Fig. S3 show the presence of Ti, C, O and Cl, which again evidence the effective synthesis of $Ti_3C_2T_x$ NSs by LiF/HCl etching, and these results are in good agreement with the EDS results shown in Fig. 2 and S2.[41] It can be noticed from the spectrum of COOH–$Ti_3C_2T_x$ NSs that the acid functionalization of $Ti_3C_2T_x$ NSs results in enhanced peak intensities for C 1s and O 1s. Fig. 4a depicts the core-level C 1s spectrum of $Ti_3C_2T_x$ NSs, wherein the peaks appearing at 283.8, 284.6, 285.6 and 288.2 eV are due to Ti–C, C═C, C═O and O–C═O, respectively.[42] It can be perceived from the C 1s spectrum (Fig. 4c) that the peaks corresponding to C═C and C═O have intensified and the peak with respect to Ti–C is diminished, which clearly indicates the increased amount of –COOH groups on COOH–$Ti_3C_2T_x$ NSs. Fig. 4b demonstrates the O 1s core-level spectrum of $Ti_3C_2T_x$ NSs, which can be further deconvoluted into three peaks attributed to Ti–O (529 eV), C═O (530 eV) and C–Ti–O_x (532 eV). Further, the fitted O 1s spectrum of COOH–$Ti_3C_2T_x$ NSs reveals a new peak at 530.6 eV (Fig. 4d), corresponding to the Ti–O–C covalent bond formation.[43] Fig. S3b and c show the core-level Ti 2p spectra of $Ti_3C_2T_x$ NSs and COOH–$Ti_3C_2T_x$ NSs, which can be deconvoluted into six peaks associated with Ti–C $2p_{3/2}$, Ti^{2+} $2p_{3/2}$, Ti–O $2p_{3/2}$, Ti–C $2p_{1/2}$, Ti^{2+} $2p_{1/2}$, and Ti–O $2p_{1/2}$, respectively.[44] All these detailed structural, morphological and spectral investigations explicitly confirm the successful synthesis and formation of $Ti_3C_2T_x$ NSs and COOH–$Ti_3C_2T_x$ NSs and the covalent anchoring of TB on COOH–$Ti_3C_2T_x$ NSs.

3.2. Electrochemical behaviour of the TB/COOH–$Ti_3C_2T_x$/GCE

In order to progressively investigate the electrochemical behaviour during the stepwise fabrication of the

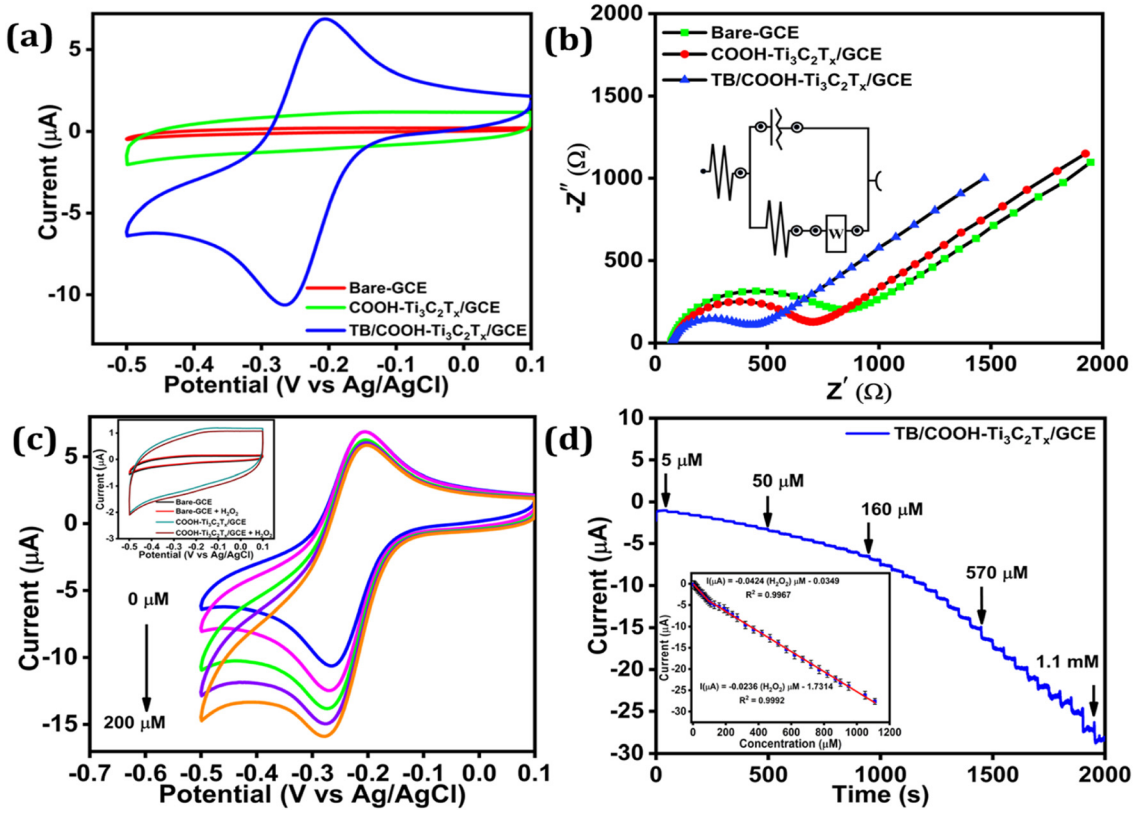

Fig. 5 (a) CV response of the bare GCE (red), COOH–$Ti_3C_2T_x$/GCE (green) and TB/COOH–$Ti_3C_2T_x$/GCE (blue) in N_2-saturated 0.1 M PBS (pH 7) at a scan rate of 20 mV s^{-1}. (b) Nyquist plots of the sequentially modified electrodes in a 0.1 M KCl solution containing 2.5 mM $[Fe(CN)_6]^{3-/4-}$. Inset: corresponding equivalent circuit (c) CVs of TB/COOH–$Ti_3C_2T_x$/GCE with increasing concentration of H_2O_2 (50, 100, 150 and 200 μM). Inset: CVs of the bare GCE and COOH–$Ti_3C_2T_x$/GCE in the absence and presence of 200 μM H_2O_2. (d) Amperometric (*i*–*t*) curve of the TB/COOH–$Ti_3C_2T_x$/GCE for the sequential addition of H_2O_2 into a constantly stirred N_2-saturated electrolyte at an applied potential of −0.25 V. Inset: calibration plot for H_2O_2 detection.

electrochemical sensor, the cyclic voltammetric (CV) response was recorded in N_2-saturated 0.1 M phosphate buffer solution (PBS) (pH 7.0) at a scan rate of 20 mV s^{-1}, and the results are displayed in Fig. 5a. As expected, the bare GCE and COOH–$Ti_3C_2T_x$/GCE did not show any redox peaks within the fixed potential window (0.1 to −0.5 V) of the investigation. However, the TB/COOH–$Ti_3C_2T_x$/GCE demonstrates a well-defined redox peak with cathodic and anodic peak potentials of −0.26 V and −0.21 V, respectively, with a formal potential of −0.24 V and a peak separation of 50 mV, corresponding to the TB redox dye. A stable redox couple with less peak separation and prominent current response is observed only for the TB/COOH–$Ti_3C_2T_x$/GCE, which may be due to the firm covalent immobilization of TB and the improved electrochemically active surface area and superior conductivity offered by the host $Ti_3C_2T_x$ NS platform.

To examine the interfacial charge transfer between the electrode and electrolyte during the stepwise TB-modified electrode fabrication, electrochemical impedance spectroscopy (EIS) was conducted in the solution containing 0.1 M KCl and 2.5 mM $[Fe(CN)_6]^{4-/3-}$. The Nyquist plot presented in Fig. 5b illustrates the impedance data, which were fitted using a Randles circuit model (inset in Fig. 5b), where the diameter of the semicircle observed in the plot corresponds to the charge transfer resistance (R_{ct}). The graph corresponding to the bare GCE reveals a significantly high R_{ct} value of 718 Ω, suggesting the pronounced inadequacy of electron transfer at the surface of the bare GCE. Upon the integration of COOH–$Ti_3C_2T_x$ NSs over the GCE, the R_{ct} notably drops to 592 Ω, emphasizing the improved conductivity imparted by COOH–$Ti_3C_2T_x$ NSs. The subsequent modification with TB in the TB/COOH–$Ti_3C_2T_x$/GCE results in a remarkably low R_{ct} of 340 Ω, highlighting the superior electron transfer efficiency facilitated by the mediator. According to the EIS results, the facile COOH–$Ti_3C_2T_x$ NS platform offers good conductivity, which makes it appropriate for electrochemical sensing. In order to examine the nature of the electrochemical process occurring at the fabricated electrochemical sensor TB/COOH–$Ti_3C_2T_x$/GCE, the scan rate effect was analysed in 0.1 M PBS by varying the scan rate from 10 mV s^{-1} to 100 mV s^{-1} (Fig. S4a). Cathodic and anodic peak currents enhance incrementally with respect to the scan rate, and the plot of current *versus* the square root of the scan rate exhibits linearity, indicating the diffusion-controlled redox process occurring at the TB-modified electrode (Fig. S4b).

3.3. Electrocatalytic activity of the TB/COOH–$Ti_3C_2T_x$/GCE towards H_2O_2 reduction

The improved electrochemical behaviour with well-defined redox peaks of the TB/COOH–$Ti_3C_2T_x$/GCE inspired us to probe its catalytic efficiency towards the electrocatalytic detection of H_2O_2. Therefore, the electrocatalytic activity of the bare GCE, COOH–$Ti_3C_2T_x$/GCE and TB/COOH–$Ti_3C_2T_x$/GCE towards H_2O_2 sensing was examined by recording CV in the presence and absence of H_2O_2 in N_2-saturated PBS (0.1 M, 7 pH). The bare (red curve) and COOH–$Ti_3C_2T_x$/GCE (brown curve) do not exhibit any electrocatalytic response upon the addition of H_2O_2 (inset, Fig. 5c), whereas the TB/COOH–$Ti_3C_2T_x$/GCE demonstrates an excellent catalytic response with increasing cathodic peak current. Fig. 5c depicts the CV response of the TB/COOH–$Ti_3C_2T_x$/GCE towards increasing H_2O_2 concentrations of 0, 50, 100, 150 and 200 μM at a scan rate of 20 mV s^{-1}. For every successive addition of H_2O_2, the cathodic peak current exhibits a linear increase at −0.25 V, while the anodic peak current displays a slight decline. This response signifies the TB-mediated electrocatalytic reduction of H_2O_2 occurring at the TB/COOH–$Ti_3C_2T_x$/GCE electrochemical sensor. During the electrocatalytic process, TB gets reduced when its reduction potential is attained. The reduced TB further reacts with H_2O_2 at the electrode–electrolyte interface, and subsequently, the TB mediator gets oxidized. These reactions (eqn (1) and (2)) repeat in a cycle as long as the analyte, H_2O_2, is available on the surface of the TB/COOH–$Ti_3C_2T_x$/GCE, which results in a stable enhancement of the cathodic current with every addition of H_2O_2.[19,45] These results confirm that COOH–$Ti_3C_2T_x$ acts as a versatile host platform for immobilizing TB, which affords remarkable electrocatalytic activity during the reduction of H_2O_2. Thus, the electrocatalytic efficacy of the TB/COOH–$Ti_3C_2T_x$/GCE sensor is attributed to the enhanced conductivity and active sites afforded by MXene and the improved electrical wiring between the TB mediator and MXene platform through the covalent immobilization of TB.

The electrochemical detection of H_2O_2 at the TB/COOH–$Ti_3C_2T_x$/GCE is represented as follows:

$$TB(Oxd) + 2e^- + 2H^+ \rightarrow TB(Red) \quad (1)$$

$$TB(Red) + H_2O_2 \rightarrow TB(Oxd) + H_2O \quad (2)$$

3.4. Amperometric determination of H_2O_2 at the TB/COOH–$Ti_3C_2T_x$/GCE

The TB/COOH–$Ti_3C_2T_x$/GCE demonstrated excellent electrocatalytic response towards H_2O_2 detection in CV investigations, which prompted us to authenticate the determination of H_2O_2 under dynamic conditions using amperometric measurements. The maximum catalytic response of the TB/COOH–$Ti_3C_2T_x$/GCE for H_2O_2 reduction was observed at −0.25 V, which was fixed as the applied potential to perform amperometric studies. Fig. 5d demonstrates the stepwise amperometric response of the TB/COOH–$Ti_3C_2T_x$/GCE at an applied potential of −0.25 V for the consecutive addition of H_2O_2 to a stirred (300 rpm) N_2-saturated PBS (0.1 M, pH 7.0) electrolyte. For every successive addition of H_2O_2 at the TB/COOH–$Ti_3C_2T_x$/GCE, an instantaneous rise in the catalytic current is observed, and it reaches its steady state current within <3 s. The corresponding calibration plot of the amperometric response was obtained by plotting the H_2O_2 concentration against the increase in the current response achieved at the TB/COOH–

$Ti_3C_2T_x$/GCE (inset, Fig. 5d). The fabricated sensor TB/COOH–$Ti_3C_2T_x$/GCE exhibits excellent catalytic response towards H_2O_2 reduction in two concentration ranges from 5 μM to 100 μM and 100 μM to 1.1 mM, after which the linearity of the calibration plot deflects gradually. Further, the LOD and sensitivities of the constructed sensor are estimated to be 1.5 μM and 0.61 μA μM^{-1} cm^{-2} and 0.33 μA μM^{-1} cm^{-2}, respectively. The obtained results are comparable or better than those for the recently reported non-enzymatic electrochemical sensors for H_2O_2 reduction, as illustrated in Table 1. The better sensitivity and enhanced catalytic activity of the TB/COOH–$Ti_3C_2T_x$/GCE are ascribed to the fast electron transfer ability of the TB mediator and the high conductivity offered by the $Ti_3C_2T_x$ NS host platform.

3.5. Interference, stability and reproducibility studies of the TB/COOH–$Ti_3C_2T_x$/GCE

The selectivity of the modified sensor towards H_2O_2 is a crucial aspect for real-time analysis, and it was assessed in the presence of other concomitant interfering analytes including ascorbic acid (AA), dopamine hydrochloride (DA), uric acid (UA), glucose (Glu), cholesterol (Chol), tryptophan (L-Tryp), cysteine (Cys), valine (Val) and potassium nitrite (KNO_2). As can be observed in Fig. 6a, only H_2O_2 injection exhibits a notable current response, and even 10 times larger concentrations of other species do not significantly change the current response (Fig. 6b). The rapid response attained during the addition of H_2O_2 is due to the enhanced electrical communication between TB and COOH–$Ti_3C_2T_x$ NSs during the covalent immobilization. Further, the selectivity of the sensor can be ascribed to the selective electrocatalytic reduction of H_2O_2 by the TB mediator at the chosen lower working potential of −0.25 V. In addition, the stability of the constructed TB/COOH–$Ti_3C_2T_x$/GCE was examined by reanalysing the stored electrochemical sensor and performing continuous potential cycling. Fifty successive cyclic voltammograms were recorded for the TB/COOH–$Ti_3C_2T_x$/GCE, and the observations are displayed in Fig. 6c. The results exhibit outstanding cycling stability with no discernible change in peak potentials and peak currents. Fig. 6c, inset displays the current response recorded at regular intervals over a 40-day storage period for the developed electrochemical sensor with and without H_2O_2. During this time, the sensor TB/COOH–$Ti_3C_2T_x$/GCE retains its initial responses of 96.4% and 93.6% in the absence and presence of H_2O_2, respectively. The sensor achieves this robust cyclic and long-term stability as an outcome of the stable immobilization strategy adapted for the water-soluble mediator TB on COOH–$Ti_3C_2T_x$. Though the $Ti_3C_2T_x$ MXenes afford excellent electrochemical properties, they tend to oxidize upon long-term exposure to ambient conditions or upon subjecting them to higher positive potentials. Thus, these sensors have to be operated at negative or lower positive potentials and have to be stored under inert conditions when not in use. Efforts to improve the stability of these MXenes through structural modulation *via* judicious interfacial engineering and also designing new MXenes with enhanced stability are underway in our laboratory. The reproducibility of the sensor was examined by fabricating various TB-modified electrodes using an identical procedure and recording their current response in the presence and absence of H_2O_2 (Fig. 6d). The results demonstrate that the fabricated batch of TB sensors has very good reproducibility with no noticeable decline in current response. The better storage and cyclic stability of the proposed electrochemical sensor can again be credited to the effective covalent immobilization of TB over the highly conductive substrate COOH–$Ti_3C_2T_x$.

3.6. Real-time detection of H_2O_2

In order to investigate the efficacy and suitability of the TB/COOH–$Ti_3C_2T_x$/GCE for real-time biological samples, H_2O_2 determination was performed by spiking a known concentration of H_2O_2 in real samples, such as diluted milk and goat serum (purchased from the local slaughterhouse), and the obtained results are displayed in Table 2. In brief, milk and serum (1 mg mL^{-1}) samples were diluted using 0.1 M PBS, and then, known concentrations of H_2O_2 were spiked by the standard addition method (Fig. S5). Also, we have compared our

Table 1 Performance of the TB/COOH–$Ti_3C_2T_x$/GCE sensor towards H_2O_2 detection compared with recently reported non-enzymatic electrochemical sensors

Electrode material	Analyte	Operating potential (V)	Linear range (μM)	LOD (μM)	Sensitivity	Ref.
$ZnFe_2O_4$/g-C_3N_4	H_2O_2	1	5–200	1	189.5 μA mM^{-1} cm^{-2}	2
MX/CS/PB/GCE	H_2O_2	0	0.05–667	0.004	—	46
CC/Nb_2CT_x@PB480	H_2O_2	−0.1	1–100	20	—	47
Co_3O_4/ATNTs	H_2O_2	−0.6	1.27–26.80	6.71	39.53 μA mM^{-1} cm^{-2}	48
Gr/P-CoHCF-NSPs	H_2O_2	0.95	1–1000	1	914 μA mM^{-1} cm^{-2}	49
MWCNT–$Ti_3C_2T_x$-Pd	H_2O_2	0	50–18 000	3.83	293.85 μA mM^{-1} cm^{-2}	50
Cu/CoO NCs	H_2O_2	−0.2	100–1000	1.85	27.7 μA mM^{-1} cm^{-2}	51
Co_3O_4 nPTLS	H_2O_2	−1.2	25–5000	5.2	201 μA mM^{-1} cm^{-2}	52
Mn_xO_y/$Ti_3C_2T_x$-GCE	H_2O_2	0.89	0.05–650	0.0045	17 420 μA mM^{-1} cm^{-2}	53
Pd–Ti_2NT_xMXene/GCE	H_2O_2	0.4	5–200	0.72	0.825 μA μM^{-1} cm^{-2}	54
CuO–CeO_2/MXene	H_2O_2	0.3	5–100	1.7	—	55
TB/COOH–$Ti_3C_2T_x$/GCE	**H_2O_2**	**−0.25**	**5–100 & 100–1100**	**1.5**	**0.61 μA μM^{-1} cm^{-2}**	**This work**

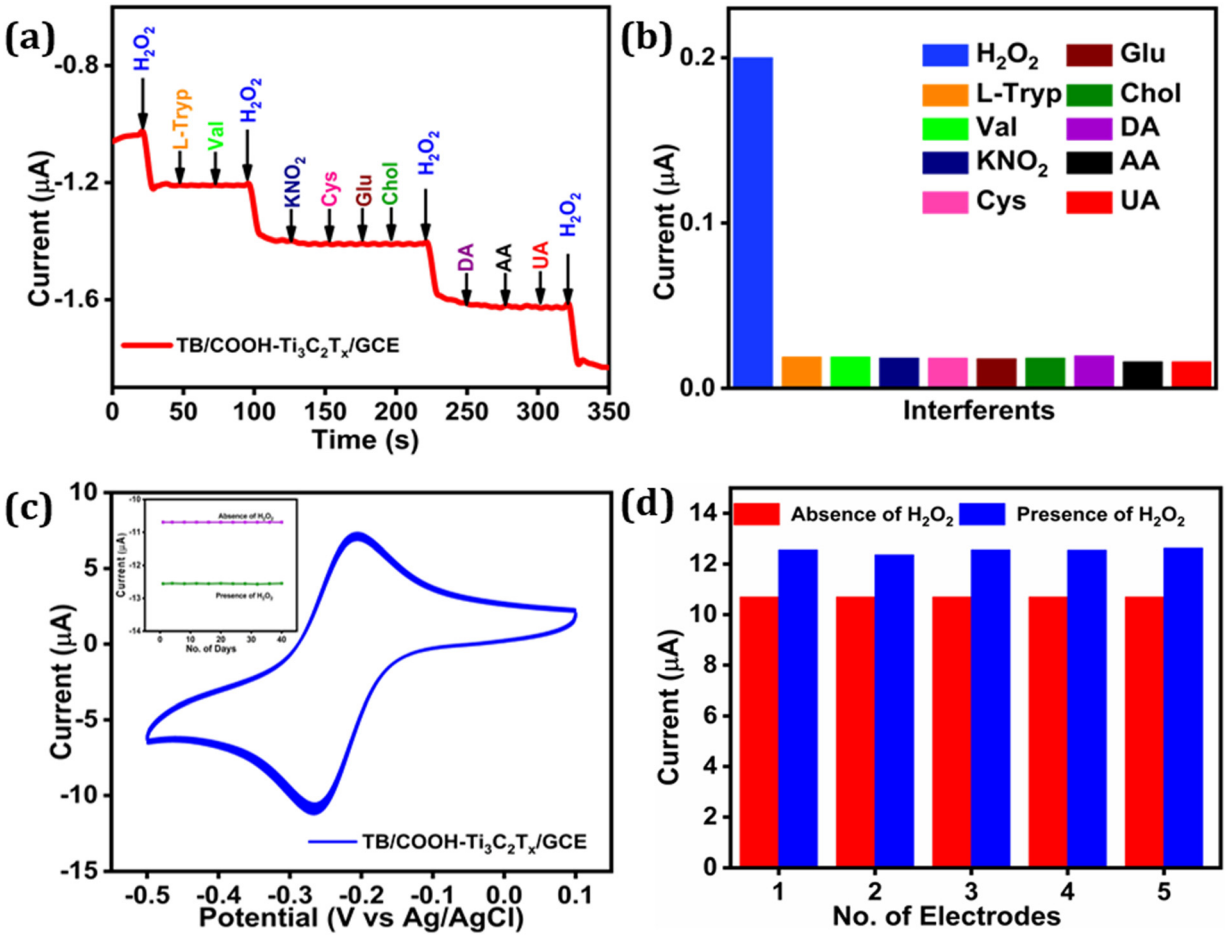

Fig. 6 (a) Effect of interference in H_2O_2 determination (5 μM) in the presence of other interferents (0.5 mM) in N_2-saturated 0.1 M PBS (pH 7) and (b) the corresponding bar diagram. (c) CV curve of the TB/COOH–$Ti_3C_2T_x$/GCE for 50 continuous cycles. Inset: the plot of day-to-day current response of the fabricated sensor in the presence (green) and absence (pink) of 50 μM H_2O_2. (d) Bar diagram comparing the current response with and without H_2O_2 (50 μM) for five identically fabricated sensors.

Table 2 Determination of H_2O_2 in real samples

Sample	Spiked (μM)	Found (μM)		Recovery ± RSD (%)
		Standard method	Our method[a]	
Milk	50	49.8	49.2	98.4 ± 1.24
	150	150.1	152.3	101.5 ± 1.02
Goat serum	50	49.9	48.9	97.8 ± 1.13
	150	151.2	153.1	102.0 ± 1.1

[a] Measurements were performed in triplicate.

results with the standard permanganate titration for H_2O_2 determination. The estimated concentrations of H_2O_2 in milk and serum samples using the constructed electrochemical sensor match very well with the added amounts and also with the standard titration method. The recovery values achieved using the constructed electrochemical sensor are between 97.8% and 102.0% with lower RSD values. These findings demonstrate that the TB/COOH–$Ti_3C_2T_x$/GCE can effectively detect H_2O_2 in real biological samples.

4. Conclusion

This report presents the design and development of an efficient electrochemical sensor for the sensitive and specific detection of H_2O_2. The $-NH_2$ groups in TB were chemically bonded to the –COOH groups in COOH–$Ti_3C_2T_x$ NSs using EDC/NHS cross-coupling chemistry. The large surface area of COOH–$Ti_3C_2T_x$ NSs not only provided a good electron tunnelling path for enhanced conductivity and sensitivity, but also served as a versatile host to offer an increased

loading of the redox mediator. The mediator TB exhibited well-defined redox behaviour with high stability and good reproducibility due to its stable covalent immobilization over COOH–$Ti_3C_2T_x$ NSs. Further, the fabricated electrochemical sensor based on the TB/COOH–$Ti_3C_2T_x$/GCE demonstrated excellent catalytic response for H_2O_2 detection at a low operating potential of −0.25 V with high selectivity. The analytical properties, like wide concentration range, low LOD, competent sensitivity and interference-free sensing, of TB/COOH–$Ti_3C_2T_x$/GCE reveal the great potential of the TB sensor in the early diagnosis of various diseases through the detection of the H_2O_2 biomarker. The prudent surface engineering of $Ti_3C_2T_x$ NSs towards the development of a non-enzymatic electrochemical sensor established in this work could open new paths for designing a broad range of devices in healthcare diagnostics.

Author contributions

Devarasu Mohanapriya: conceptualization, methodology, investigation, validation, writing – original draft. Kathavarayan Thenmozhi: conceptualization, resources, supervision, project administration, writing – review & editing.

Conflicts of interest

There are no conflicts to declare.

Data availability

See DOI: **https://doi.org/10.1039/D5SD00114E**. Supplementary information: materials, instrumentation, FESEM image and elemental analysis of Ti_3AlC_2 and $Ti_3C_2T_x$ NSs, XPS survey spectra of $Ti_3C_2T_x$ NSs and COOH–$Ti_3C_2T_x$ NSs, Core level spectrum of Ti 2p in $Ti_3C_2T_x$ NSs and COOH–$Ti_3C_2T_x$ NSs, Effect of scan rate and corresponding calibration plot, real-time analysis.

The data supporting this article have been included as part of the SI. The original files will be made available on request.

Acknowledgements

This work was financially supported by Vellore Institute of Technology (VIT) Vellore under the Faculty Seed Grant (RGEMS) (Sanction Order No.: SG20220001). The authors also acknowledge the Central Research Facilities (CRF), Vellore Institute of Technology (VIT), for providing instrumentation facilities.

References

1 R. Banavath, R. Srivastava and P. Bhargava, *ACS Appl. Nano Mater.*, 2021, **4**, 5564–5576.
2 M. Ye, C. Yang, Y. Sun, J. Wang, D. Wang, Y. Zhao, Z. Zhu, P. Liu, J. Zhu, C. Li, W. Peng, N. Zhang and Y. Dong, *ACS Appl. Nano Mater.*, 2022, **5**, 10922–10932.
3 X. Chai, S. Ye, F. Wang, H. Yuan, M. Liu, F. Fan, L. Zhang, X. Zhang, T. Wang and Y. Fu, *Inorg. Chem.*, 2023, **62**, 10694–10703.
4 Z. Yang, Z. Tian and C. Qi, *ACS Appl. Nano Mater.*, 2023, **6**, 21141–21151.
5 J. E. Giaretta, H. Duan, F. Oveissi, S. Farajikhah, F. Dehghani and S. Naficy, *ACS Appl. Mater. Interfaces*, 2022, **14**, 20491–20505.
6 W. Chen, S. Cai, Q. Q. Ren, W. Wen and Y. Di Zhao, *Analyst*, 2012, **137**, 49–58.
7 V. P. Sruthi, S. Sarfudeen, T. Panda, K. Thenmozhi and S. Senthilkumar, *J. Mater. Chem. A*, 2025, **13**, 8343.
8 V. P. Sruthi and S. Senthilkumar, *J. Mater. Chem. C*, 2024, **12**, 8924–8934.
9 D. Mohanapriya and K. Thenmozhi, *J. Mater. Chem. B*, 2025, **13**, 2306.
10 A. Sugunan, A. V. Rethnakumaran and M. M. Menamparambath, *Sens. Diagn.*, 2024, **3**, 1769–1788.
11 J. Liu, M. Li, W. Liu, Z. Hao, F. Zhang, H. Pang, R. Zhang and L. Zhang, *J. Electroanal. Chem.*, 2024, **954**, 118060.
12 B. Luo, X. Li, J. Yang, X. Li, L. Xue, X. Li, J. Gu, M. Wang and L. Jiang, *Anal. Methods*, 2014, **6**, 1114–1120.
13 J. Guo, S. Li, J. Wang and J. Wang, *Biosens. Bioelectron.*, 2022, **198**, 113820.
14 S. Liu, B. Yu, T. Fei and T. Zhang, *Sens. Actuators, B*, 2014, **201**, 240–245.
15 C. Bruckschlegel, V. Fleischmann, N. Gajovic-Eichelmann and N. Wongkaew, *Talanta*, 2025, **291**, 127850.
16 H. Wu, W. Zheng, Y. Jiang, J. Xu and F. Qiu, *New J. Chem.*, 2021, **45**, 21676–21683.
17 A. Emin, A. Ding, S. Ali, M. Chhattal, S. Ali, A. Parkash and Q. Li, *Microchem. J.*, 2024, **207**, 111972.
18 R. Peng, A. Offenhäusser, Y. Ermolenko and Y. Mourzina, *Sens. Actuators, B*, 2020, **321**, 128437.
19 K. Thenmozhi and S. Sriman Narayanan, *Anal. Bioanal. Chem.*, 2007, **387**, 1075–1082.
20 E. Martínez-Periñán, A. Domínguez-Saldaña, A. M. Villa-Manso, C. Gutiérrez-Sánchez, M. Revenga-Parra, E. Mateo-Martí, F. Pariente and E. Lorenzo, *Sens. Actuators, B*, 2023, **374**, 132761.
21 A. Esokkiya, S. Sudalaimani, K. Sanjeev Kumar, P. Sampathkumar, C. Suresh and K. Giribabu, *ACS Omega*, 2021, **6**, 9528–9536.
22 D. Manoj, K. Theyagarajan, D. Saravanakumar, S. Senthilkumar and K. Thenmozhi, *Biosens. Bioelectron.*, 2018, **103**, 104–112.
23 M. Zhang and W. Gorski, *J. Am. Chem. Soc.*, 2005, **127**, 2058–2059.
24 Y. M. Liu, C. Punckt, M. A. Pope, A. Gelperin and I. A. Aksay, *ACS Appl. Mater. Interfaces*, 2013, **5**, 12624–12630.
25 X. Liang, Y. Zhou, J. M. S. Almeida and C. M. A. Brett, *J. Electroanal. Chem.*, 2023, **936**, 117366.
26 H. Wang, Q. Dong, L. Lei, S. Ji, P. Kannan, P. Subramanian and A. P. Yadav, *Nanomaterials*, 2021, **11**, 20857.
27 P. Kanagavalli, C. Andrew, M. Veerapandian and M. Jayakumar, *TrAC, Trends Anal. Chem.*, 2021, **143**, 116413.

28 K. Sakthivel, S. Balasubramanian, G. P. Chang-Chien, S. F. Wang, Ahammad, W. Billey, J. Platero, T. Soundappan and P. Sekhar, *ECS Sens. Plus*, 2024, **3**, 020605.
29 S. Ullah, T. Najam, A. ur Rehman, S. S. Alarfaji, M. A. Ahmad, S. Riaz, B. Akkinepally, S. S. A. Shah and M. A. Nazir, *J. Alloys Compd.*, 2024, **1001**, 175172.
30 D. Mohanapriya, J. Satija, S. Senthilkumar, V. Kumar Ponnusamy and K. Thenmozhi, *Coord. Chem. Rev.*, 2024, **507**, 215746.
31 A. Vahidmohammadi, J. Moncada, H. Chen, E. Kayali, J. Orangi, C. A. Carrero and M. Beidaghi, *J. Mater. Chem. A*, 2018, **6**, 22123–22133.
32 S. B. Ambade, L. A. Kesner, M. K. Abdel-Rahman, D. H. Fairbrother and Z. Rosenzweig, *ACS Appl. Nano Mater.*, 2023, **6**, 4898–4909.
33 X. Liu, Y. Qiu, D. Jiang, F. Li, Y. Gan, Y. Zhu, Y. Pan, H. Wan and P. Wang, *Microsyst. Nanoeng.*, 2022, **8**, 35.
34 M. Alhabeb, K. Maleski, B. Anasori, P. Lelyukh, L. Clark, S. Sin and Y. Gogotsi, *Chem. Mater.*, 2017, **29**, 7633–7644.
35 A. P. Isfahani, A. A. Shamsabadi, F. Alimohammadi and M. Soroush, *J. Hazard. Mater.*, 2022, **434**, 128780.
36 S. Shah, I. Mubeen, E. Pervaiz and H. Nasir, *FlatChem*, 2023, **41**, 100544.
37 P. Najmi, N. Keshmiri, M. Ramezanzadeh, B. Ramezanzadeh and M. Arjmand, *Chem. Eng. J.*, 2023, **456**, 141001.
38 K. Wang, L. Shen, Q. Zhu, R. Bo, R. Lu, X. Lu and Z. Fu, *Chem. Eng. J.*, 2023, **452**, 139156.
39 I. M. Chirica, A. G. Mirea, T. Şuteu, A. Kuncser, Ş. Neațu, M. Florea, M. W. Barsoum and F. Neațu, *ACS Sustainable Chem. Eng.*, 2024, **12**, 9766–9776.
40 B. Scheibe, K. Tadyszak, M. Jarek, N. Michalak, M. Kempiński, M. Lewandowski, B. Peplińska and K. Chybczyńska, *Appl. Surf. Sci.*, 2019, **479**, 216–224.
41 C. Roy, S. K. De, P. Banerjee, S. Pradhan and S. Bhattacharyya, *J. Alloys Compd.*, 2023, **938**, 168471.
42 L. He, L. Wang, L. Yang, J. Cui, X. Jiang, Y. Ge, J. Zhang, J. Yang, Q. Hou and J. Shen, *ACS Appl. Nano Mater.*, 2024, **7**, 14769–14779.
43 B. S. Shen, H. Wang, L. J. Wu, R. S. Guo, Q. Huang and X. Bin Yan, *Chin. Chem. Lett.*, 2016, **27**, 1586–1591.
44 A. Pazniak, P. Bazhin, N. Shplis, E. Kolesnikov, I. Shchetinin, A. Komissarov, J. Polcak, A. Stolin and D. Kuznetsov, *Mater. Des.*, 2019, **183**, 108143.
45 P. Yaiwong, K. Iamsawat, S. Wiratchan, W. Jumpathong, N. Semakul, S. Bamrungsap, J. Jakmunee and K. Ounnunkad, *Food Chem.*, 2024, **439**, 138147.
46 F. Zhu, X. Wang, X. Yang, C. Zhao, Y. Zhang, S. Qu, S. Wu and W. Ji, *Anal. Methods*, 2021, **13**, 2512–2518.
47 A. Mohan Arjun, N. Shabana, M. Ankitha and P. Abdul Rasheed, *Microchem. J.*, 2023, **185**, 108301.
48 R. Ullah, M. A. Rasheed, S. Abbas, K. ul Rehman, A. Shah, K. Ullah, Y. Khan, M. Bibi, M. Ahmad and G. Ali, *Curr. Appl. Phys.*, 2022, **38**, 40–48.
49 R. Banavath, R. Srivastava and P. Bhargava, *Catal. Sci. Technol.*, 2022, **12**, 2369–2383.
50 J. Zhang, M. Lu, H. Zhou, X. Du and X. Du, *Int. J. Mol. Sci.*, 2022, **23**, 13.
51 C. Liu, J. Choi, J. Hyun, S. H. Bhang and T. Yu, *Korean J. Chem. Eng.*, 2023, **40**, 2771–2777.
52 V. Gerbreders, M. Krasovska, E. Sledevskis, I. Mihailova and V. Mizers, *Micromachines*, 2024, **15**, 311.
53 B. Wanga, S. M. Khoshfetrat and H. Mohamadimanesh, *Microchem. J.*, 2024, **207**, 111796.
54 Y. Zhang, L. He, X. Sun, C. Yang and J. Li, *ChemistrySelect*, 2024, **9**, 44.
55 K. Zhou, Y. Li, S. Zhuang, J. Ren, F. Tang, J. Mu and P. Wang, *J. Electroanal. Chem.*, 2022, **921**, 116655.